Directed Emission from Self-Assembled Microhelices

*Lukas Helmbrecht, Melissa Tan, Ruslan Röhrich, Marloes H. Bistervels, Bruno Ortiz Kessels, A. Femius Koenderink, Bart Kahr, Willem L. Noorduin**

L. H., R. R., M. H. B., B. O. K., Prof. Dr. A. F. K., Dr. W. L. N.
AMOLF, Science Park 104, 1098XG Amsterdam, The Netherlands
E-mail: noorduin@amolf.nl

R. R.
ARCNL, Science Park 106, 1098XG Amsterdam, The Netherlands

M. T., Prof. Dr. B. K.
Department of Chemistry, New York University, 100 Washington Square East, New York City, New York 10003-6688, USA.

Keywords: self-assembly, bioinspired materials, hierarchical structures, polarimetry, optical microscopy

Bottom-up assembly can organize simple building blocks into complex architectures for light manipulation. The optical properties of self-assembled polycrystalline barium carbonate/silica double helices are studied using fluorescent Fourier and Mueller matrix microscopy. Helices doped with fluorescein direct light emission along the long axis of the structure. Furthermore, light transmission measured normal and parallel to the long axis exhibits twist sense-specific circular retardance (CR) and wave-guiding, respectively, albeit the measurements suffer from depolarization. The helices thus integrate highly directional emission with enantiomorph-specific polarization. This optical response emerges from the arrangement of nanoscopic mineral crystallites in the microscopic helix, and demonstrates how bottom-up assembly can achieve ordering across multiple length scales to form complex functional materials.

1. Introduction

Material syntheses based on self-assembly have given rise to structures with unique mechanical, magnetic, electric and optical properties.[1–6] Such bottom-up assembly strategies also enable hierarchical ordering of building blocks across multiple length scales, thereby offering the opportunity to integrate multiple functionalities within a single material.

Helical-shaped nanocomposites formed from barium carbonate ($BaCO_3$) nanocrystals and amorphous silica (SiO_2) can put these ideas to the test. These bioinspired nanocomposites have been observed to self-assemble into highly intricate, yet controllable, three-dimensional (3D) shapes such as vases, stems, and helices, that can be further sculpted and chemically modified.[7–18] The structural layout of the helical composites has been studied in great detail: the rod-shaped nanocrystals are elongated along their *c*-axes and align parallel to one another while precessing tangentially around the helical axis, [8–18] thus forming a chiral ensemble as shown in **Figure 1**.

It is well-known that chiral assemblies of achiral building blocks can exhibit handedness-specific optical responses.[19,20] Hence, the intricately ordered, anisotropic medium of the helices suggests that these architectures may have optical properties absent in their building blocks alone. The twisting matrix overlays linearly birefringent nanocrystals of $BaCO_3$ (n_α = 1.529, n_β = 1.676, n_γ = 1.677) in multiple directions with respect to incident wave vectors.[21,22] Moreover, the high refractive indices of the $BaCO_3/SiO_2$ ($n \sim 1.5$) medium may also affect total internal reflection and wave guiding at some optical frequencies.[13,23] These expectations are evaluated in by studying the optical properties of helices using fluorescent Fourier microscopy and Mueller matrix microscopy.[24,25]

2. **Results and Discussion**

2.1. Analyzing Directed Emission

$BaCO_3/SiO_2$ helices were synthesized according to a previously developed co-precipitation reaction (see Experimental Section for details).[14] After growth of 1.5 hours, typical helices were approximately 40 μm long and 5 μm wide with a pitch of about 10 μm. Fluorescein was incorporated during growth to enable active light emission.[13] If a helix behaves as a wave-guide, scattered light within should be directed to the tip. We investigated the directional emission of individual helices with respect to its orientation, characterized by a polar tilt and

azimuthal rotation (Θ_H and Φ_H, respectively) relative to a glass cover slip substrate **(Figure 2)**. These angles can be measured directly by scanning electron microscopy (SEM) (see Supporting Information (SI), section 2).

The direction of emitted light was determined using a home-built Fourier or *k*-space microscope (Figure 2a, SI section 1).[26] The base of the helix was excited with a laser (λ = 490 nm). The emission (λ_E = 510 nm) was collected with a high numerical aperture objective (NA = 0.9), whose back focal plane (Fourier plane) was projected onto a CCD camera, where each pixel position in the image corresponds to an angle of incident light in real space (Figure 2a,c). Isotropic emission would give a diffuse Fourier image, whereas directed emission would produce a focused spot.

The polar emission angle (Θ_E) is calculated as distance of the emission peak (r_E) from the center of the Fourier plane (Figure 2c):

$$\Theta_E = arcsin\left(\frac{r_E}{f}\right), \quad (1)$$

where f is the focal length of the microscope objective (see SI section 1.2 for derivation of equation (1)). This enables a direct comparison of the tilt direction of the helix, as determined by SEM, with the direction of the emitted beam. Additionally, equation (1) gives the expected emission position in the Fourier plane from the polar tilt.

We analyzed the light emission for multiple helices (Figure 2a, SI section 1). All structures show directional emission as indicated by a well-defined spot in the Fourier plane. We define the position of the light spot as the location of maximum intensity (Figure 2c), and compare the direction of the emission with the orientation of the helices previously determined by SEM. As expected, rotating the sample led to a rotation of the spot in the Fourier plane. By combining the Fourier and SEM characterization, we found a close agreement between the emission

direction (Θ_E = 40° and Φ_E = 30°) and the orientation of the helix (Θ_H = 44° and Φ_H = 26°) (Figure 2c).

Spot sizes were characterized in terms of the beaming half-angle (*i.e.* half the dispersion of the emission spot in the Fourier plane). This was 7.5° in the polar direction (Θ) and 11.5° in the azimuthal direction (Φ) (Figure 2c). A theoretical lower boundary of the beaming half-angle determined from a wave propagation simulation was 4° for light passing through a 2 µm diameter circular aperture, which is comparable to the smallest feature of the tip of the helix (SI section 1.4).[27] The experimentally found beaming half-angle is close to the theoretical limit. The microscale morphology of the helix thus determines direction and dispersion of light emission.

2.2. Analyzing Circular Birefringence

Furthermore, we analyzed the optical polarization characteristics of enantiomorphous helices. The change in polarization of light transmitted through the helices can be measured using Mueller matrix polarimetry (**Figure 3a**). The instrument design is based on dual continuously rotating waveplates.[28–31] The polarization state of light incident on the sample is modulated by coupling a stationary linear polarizer to a rotating quarter-waveplate. The polarization state of light transmitted by the sample is subsequently analyzed by passing the beam through a rotating quarter-waveplate followed by a stationary polarizer. The time-dependent light intensity signal produced by the combination of polarization state generator (PSG) and polarization state analyzer (PSA) can be inverted to recover the Mueller matrix (**M**), a 4 × 4 real-valued transformation matrix that describes the optical properties of a sample.

Light of any polarization state can be described by the Stokes vector (*S*), a four-element vector defined as $S = [I \quad Q \quad U \quad V]^T$ where *I* is the total intensity, *Q* is the difference in intensity of light polarized along the *x* and *y* directions, *U* is the intensity difference of light polarized along

$\pm$45°, and *V* is the difference in intensity between left and right circularly polarized light. An input Stokes vector (S_{in}) can be transformed to an output Stokes vector (S_{out}) by **M**, so that $S_{out} = \mathbf{M}S_{in}$.

Circular retardance (CR), the angle by which the polarization vector of light is rotated when transmitted through a sample (range: $\pm\pi$), can be evaluated from the differential Mueller matrix, which is approximated from the matrix logarithm (**L**) of **M**:[28,32,33]

$$\mathbf{L} = \begin{bmatrix} -\mathrm{A} & -\mathrm{LE} & -\mathrm{LE}' & \mathrm{CE} \\ \mathrm{LE} & -\mathrm{A} & \mathrm{CR} & \mathrm{LR}' \\ \mathrm{LE}' & -\mathrm{CR} & -\mathrm{A} & -\mathrm{LR} \\ \mathrm{CE} & -\mathrm{LR}' & \mathrm{LR} & -\mathrm{A} \end{bmatrix}. \quad (2)$$

The process of obtaining **L** unscrambles mixed linear and circular anisotropies, providing a phenomenological understanding of the polarization transformations affected by the helices (Figure 3b-e). Although this analysis is of limited utility when encountering depolarization, it is in this case a signature of the respective enantiomorphs.[34]

Ms were measured for helices whose long axes were parallel or orthogonal with respect to the light propagation direction. Measurements were collected at normal incidence transmission for a series of helices at a wavelength of 550 nm, which lies outside of the absorption band of fluorescein (SI section 2). Viewed perpendicular to the helical axis, the rope-like strands of the double helix are overlaid every half period by an angle of ~70°. Light propagating orthogonally through a left-handed helix, experiences a right-handed progression of anisotropic lamellae (Figure 3b) (as viewed from the detector). This generates a +CR; in other words, the incident plane of polarization is rotated clockwise (applying the normal convention for optical rotation whereby a dextrorotatory structure produces a clockwise rotation when looking at the light source). The converse is also true. In a right-handed helix, light encounters a left-handed arrangement of elements producing a levorotation (−CR) (Figure 3c). The maximum rotation in orthogonal transmission (up to 1.4 rad) was observed where the sample thickness is greatest (ca. 6 µm).

The CR observed in Figure 3b-c can be understood from the ordering of nanocrystals within the helix, in particular the misorientation of anisotropic nanoparticles along the wave vector as it traverses the material. Skewed stacks of anisotropic lamellae are known as Reusch piles, after the scientist who used plates of mica to mimic the action of α-quartz on the azimuth of linearly polarized light passed along the optic axis.[19,20] Dispersion theory predicts that the sense of optical rotation depends on whether the wavelength of the illumination is greater or less than the helical pitch (*P*) of the structure. Here, *P* is greater than 550 nm. Therefore, we expect that for a right-handed structure, the CR will be dextrorotary (positive) which is consistent with the experiment. The systematic dextrorotatory (red) signal in the false color micrograph of Figure 3c is likely a consequence of the inclination of this helix out of the sample plane compared with Figure 3b.

Measurements along the helical axis suffer from strong depolarization, which can be described using the degree of polarization (DOP):

$$DOP = \frac{\sqrt{Q^2+U^2+V^2}}{I^2}. \quad (3)$$

The low DOP values observed are a consequence, in part, of mismatched indices of refraction between the material and its surroundings (air); helices became dislodged when embedded in an index matching medium. Due to the low DOP, results have to be interpreted with care. Nevertheless, it is significant that the polarization responses were opposite for heterochiral helices. This provides a clue as to how the light is responding when traveling along the long axis. We presume that the helices behave as waveguides when light is transmitted through the tip; in other words, the sense of the light rotation follows the twist of the structure as in a cholesteric or twisted nematic liquid crystal.[35] Thus, a left-handed helix (Figure 3d), which rotates the plane of polarization clockwise, operates as a dextrorotary waveguide while a right-handed helix operates as a levorotatory waveguide (Figure 3e). Similar optical effects have been measured in twisted optical fibers, supporting the conclusion that nanocomposite helices of

$BaCO_3/SiO_2$ function as waveguides.[36,37] When subjected to an elastooptic deformation, monomode fibers generate a CR of opposite handedness to the twist. A right-handed deformation produces a levorotation.

3. Conclusion

Self-assembled, microscopic $BaCO_3/SiO_2$ double helices display directional emission and enantiomorph-specific circular retardance (CR). Currently, the handedness and directionality of helices are set by spontaneous symmetry breaking that occurs in the early stages of the assembly process.[38] An exciting step forward would be to program the chirality and orientation of structures on the substrate surface by deliberately steering the assembly using top-down fabrication strategies and chiral auxiliaries.[39][40]

In conclusion, helices emit highly directional light along their long axes, while affecting a differential refraction of left and right circularly polarized light. Normal to the helix axis, a CR is recorded that is best interpreted as a consequence of overlaid, misoriented, anisotropic lamellae. CR and directional emission originate from hierarchical ordering in helices, which intrinsically emerges from self-assembly. Overall, these results demonstrate the potential of bottom-up processes to organize simple building blocks across multiple length scales for complex functional materials.

4. Experimental Section

Growth of $BaCO_3$ /SiO_2 Microhelices: Typically, 0.074 mg $BaCl_2$ and 0.016 g Na_2SiO_3 (Sigma Aldrich) were dissolved in 15 mL water. The pH was adjusted to 11.2 using HCl, and 21 mg of fluorescein were added. Glass substrates of 20 x 24 x 1 mm were mounted in a 100 mL beaker, and partially immersed with the growth solution before covering with a Petri dish. After 1.5 h the glass substrates were removed and carefully rinsed with deionized water to isolate the

microhelices. This procedure yields ca. 40 μm ensembles. These helices were found to be long enough for studying the optical effects of multiple twists, yet robust for transport.

Geometric Analysis of Microhelices Using Scanning Electron Microscopy: The orientation of each microhelix was determined relative to the substrate using a FEI Verios 460 scanning electron microscope. The polar angle Θ_H was determined by orienting the sample stage such that the microhelix was parallel to the electron beam (Figure S1d).

Mueller Matrix Microscopy: The Mueller Matrix (**M**) connects an input Stokes vector (S_{in}) to its output (S_{out}): $\mathbf{M}S_{in} = S_{out}$. Herein, **M** of individual helices is measured by an imaging system based on dual continuously rotating retarders (*i.e.* waveplates). The concept is explained in the SI, the technical details of our instrument are published in full elsewhere. [29–31]

Supporting Information
Supporting Information is available from the Wiley Online Library or from the author.

Acknowledgements
The authors would like to thank Prof. Dr. J. M. García-Ruiz for fruitful discussions. This work is part of the vernieuwingsimpuls Vidi research program “Shaping up materials” with project number 016.Vidi.189.083, which is partly financed by the Dutch Research Council (NWO). Scanning electron microscopy was partially performed at the fabrication and characterization facilities of the Amsterdam nanoCenter, supported by NWO. This work was supported secondarily by the New York University Materials Research Science and Engineering Center (MRSEC) program DMR-1420073. MT acknowledges support from The Margaret and Herman Sokol Fellowship. The authors declare no conflict of interests.

Received: ((will be filled in by the editorial staff))
Revised: ((will be filled in by the editorial staff))
Published online: ((will be filled in by the editorial staff))

References

[1] G. M. Whitesides, B. Grzybowski, *Science* **2002**, *295*, 2418.

[2] K. Lee, W. Wagermaier, A. Masic, K. P. Kommareddy, M. Bennet, I. Manjubala, S. W. Lee, S. B. Park, H. Cölfen, P. Fratzl, *Nat. Commun.* **2012**, *3*, 725.

[3] H. Cölfen, S. Mann, *Angew. Chemie - Int. Ed.* **2003**, *42*, 2350.

[4] F. Nudelman, N. A. J. M. Sommerdijk, *Angew. Chemie - Int. Ed.* **2012**, *51*, 6582.

[5] A. R. Studart, *Adv. Mater.* **2012**, *24*, 5024.

[6] F. C. Meldrum, H. Cölfen *Chem. Rev.* **2008**, *108*, 4332.

[7] The resemblance of some of these shapes with structures that were identified as microfossils, has lead Garcia-Ruiz et al. to coin the term “biomorphs”. Note that these shapes are completely developed in the absence of organic molecules.

[8] J. M. Garcia-Ruiz, *J. Cryst. Growth* **1985**, *73*, 251.

[9] J. M. Garcia-Ruiz, E. Melero-Garcia, S. T. Hyde, *Science* **2009**, *323*, 362.

[10] M. Kellermeier, H. Cölfen, J. M. García-Ruiz, *Eur. J. Inorg. Chem.* **2012**, 5123.

[11] E. Bittarello, D. Aquilano, *Eur. J. Mineral.* **2007**, *19*, 345.

[12] P. Knoll, O. Steinbock *Isr. J. Chem.* **2018**, *58*, 682.

[13] C. N. Kaplan, W. L. Noorduin, L. Li, R. Sadza, L. Folkertsma, J. Aizenberg, L. Mahadevan, *Science* **2017**, *1399*, 1395.

[14] W. L. Noorduin, A. Grinthal, L. Mahadevan, J. Aizenberg, *Science* **2013**, *340*, 832.

[15] T. Holtus, L. Helmbrecht, H. C. Hendrikse, I. Baglai, S. Meuret, G. W. P. Adhyaksa, E. C. Garnett, W. L. Noorduin, *Nat. Chem.* **2018**, *10*, 740.

[16] J. Opel, F. P. Wimmer, M. Kellermeier, H. Cölfen, *Nanoscale Horizons* **2016**, *1*, 144.

[17] J. Opel, N. Unglaube, M. Wörner, M. Kellermeier, H. Cölfen, J. M. García-Ruiz,

Crystals **2019**, *9*, 1.

[18] J. Opel, J. Brunner, R. Zimmermanns, T. Steegmans, E. Sturm, M. Kellermeier, H. Cölfen, J. García-Ruiz, *Adv. Funct. Mater.* **2019**, *29*, 1902047.

[19] E. Reusch, *Ann. Phys.* **1869**, *214*, 628.

[20] G. Joly, J. Billard, J. Opt. 1981, 12, 323.

[21] E. A.-M. E. Kenneth W. B. Richard A. B., B. G.N., *Handbook of Mineralogy Crystal Data*, Mineralogical Society of America, Chantilly, VA 20151-1110, USA **2010**.

[22] K. F. Lindman, *Ann. Phys.* **1920**, *368*, 621.

[23] E. D. Palik, *Handbook of optical constants of solids*, Academic Press San Diego, CA, USA **1985**.

[24] S. Nichols, O. Arteaga, A. Martin, B. Kahr, *J. Opt. Soc. Am. A* **2015**, *32*, 2049.

[25] O. Arteaga, J. Freudenthal, B. Wang, B. Kahr, *Appl. Opt.* **2012**, *51*, 6805.

[26] A. Mohtashami, C. I. Osorio, A. F. Koenderink, *Phys. Rev. Appl.* **2015**, *4*, 1.

[27] G. Vdovin, F. van Goor, *LightPipes: beam propagation toolbox*, OKO Technologies, Delft, The Netherlands **1999**.

[28] R. M. A. Azzam, *J. Opt. Soc. Am.* **1978**, *68*, 1756.

[29] D. H. Goldstein, *Appl. Opt.* **1992**, *31*, 6676.

[30] C. Chen, I. An, G. M. Ferreira, N. J. Podraza, J. A. Zapien, R. W. Collins, *Thin Solid Films* **2004**, *455–456*, 14.

[31] S. M. Nichols, *PhD Thesis: Coherence in Polarimetry*, New York University, September **2017**.

[32] J. H. Freudenthal, E. Hollis, B. Kahr, *Chirality* **2009**; *21*, E20.

[33] O. Arteaga, B. Kahr, *J. Opt. Soc. Am. B* **2019**, *36*, F72.

[34] R. Ossikovski, A. De Martino, J. Opt. Soc. Am. A 2015, 32, 343.

[35] C. V. Mauguin, *Bull. la Société française minéralogie* **1911**, *34*, 71.

[36] R. Ulrich, A. Simon, *Appl. Opt.* **1979**, *18*, 2241.

[37] A. M. Smith, *Appl. Opt.* **1980**, *19*, 2606.

[38] The ratio between left- and right-handed helices during a typical experiment is close to racemic.

[39] J. Aizenberg, D. A. Muller, J. L. Grazul, D. R. Hamann, *Science* **2003**, *299*, 1205.

[40] W. Jiang, M. S. Pacella, D. Athanasiadou, V. Nelea, H. Vali, R. M. Hazen, J. J. Gray, M. D. McKee, *Nat. Commun.* **2017**, *8*, 1.

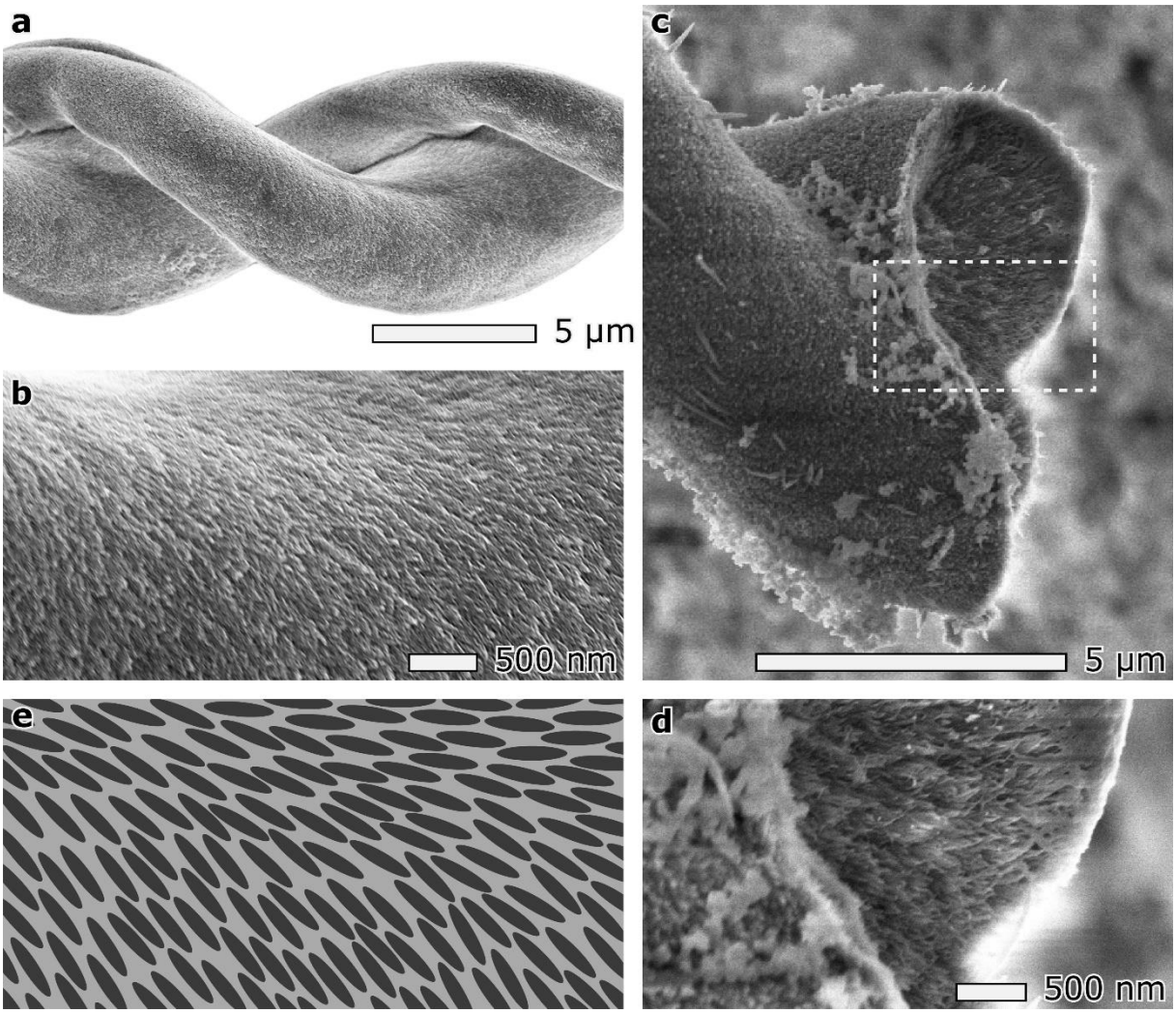

Figure 1. Visualization of the hierarchical organization of $BaCO_3/SiO_2$ helices. a) Electron micrograph of the microscale helical shape. b) The nanoscale twisting of the crystals on the outside of the helix. c) A cross-sectioned helix at higher magnification, d) showing the internal ordering of the nanocrystals. e) Schematic of the aligned nanocrystals.

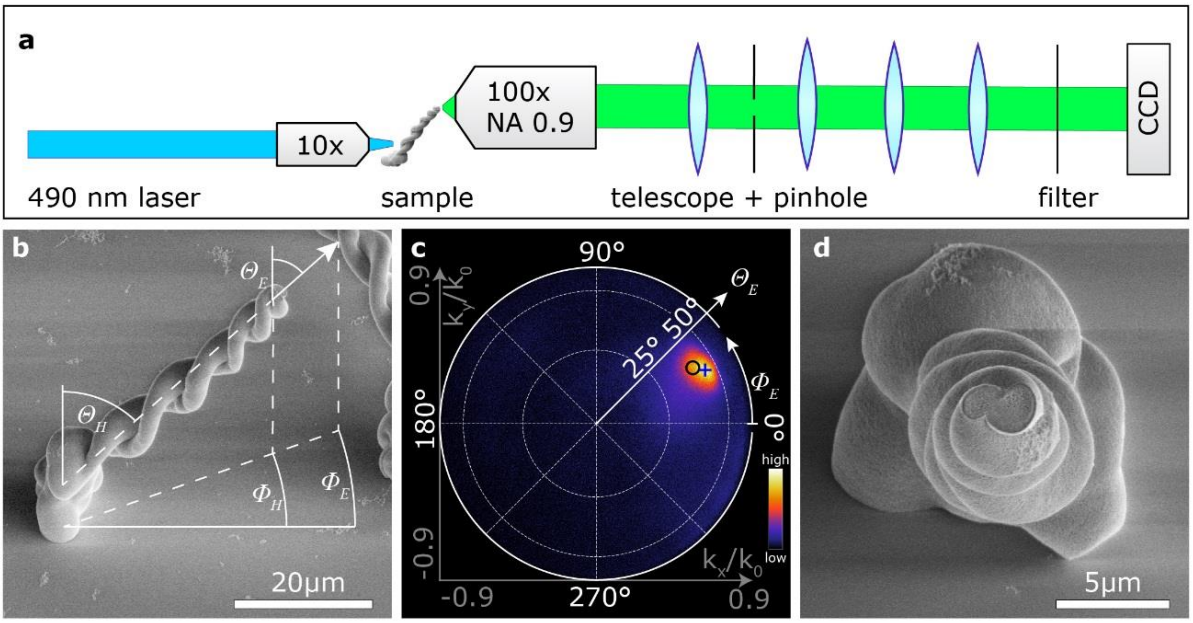

Figure 2. Directional light emission of self-assembled microhelices. a) Schematic of the Fourier microscopy setup. b) SEM image of a helix with polar tilt (Θ_H) and azimuthal rotation (Φ_H) relative to the substrate, compared with the polar angle of the emission (Θ_E) and the azimuthal rotation (Φ_E). c) Corresponding Fourier image of the emission, showing good agreement between orientation of the helix (marked with ○) and the direction of the emission (marked with +) (deviation of + 4° in Θ and - 4° in Φ). The outer circle corresponds to the maximum collection angle of 64.2° as given by the objective NA of 0.9. d) Top view of the helix showing the diameter and morphology of the tip.

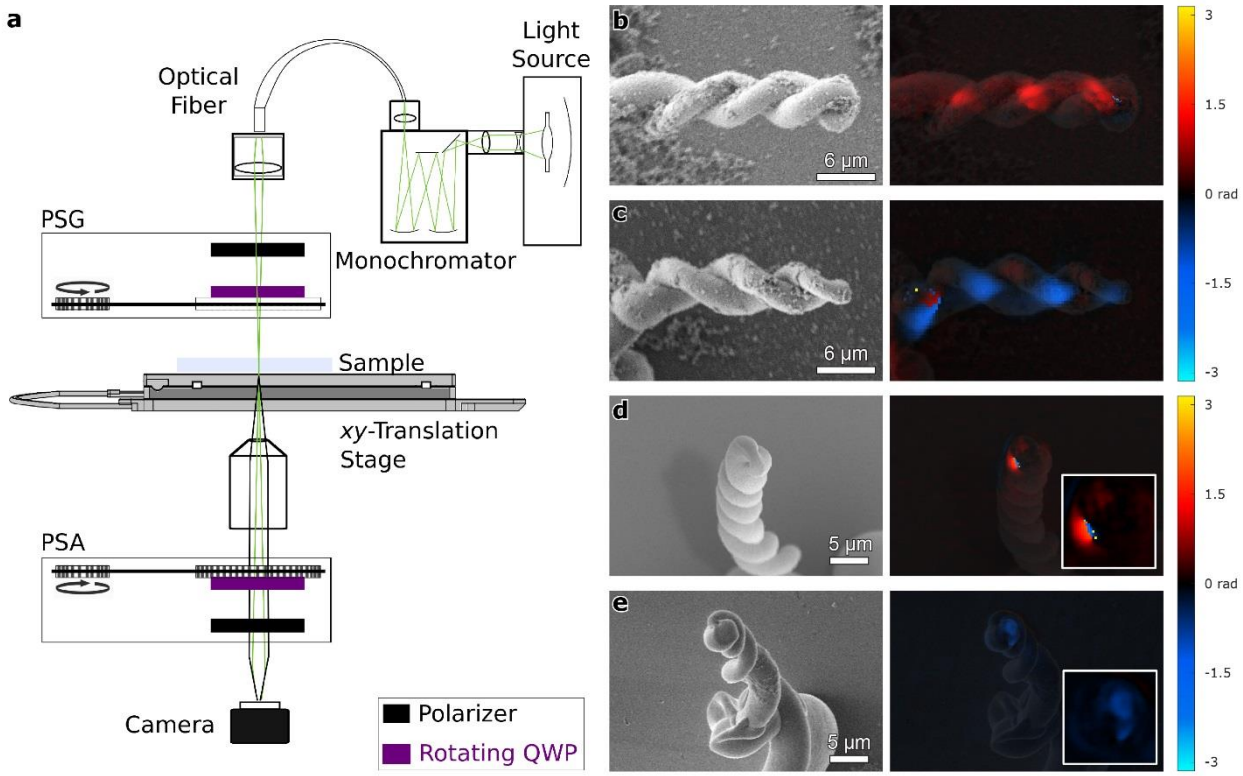

Figure 3. Circular retardance (CR) from $BaCO_3/SiO_2$ helices. a) Schematic of the Mueller Matrix microscope setup. b-c) Series of electron micrographs with CR overlaid on SEM image. A right-handed arrangement of strands (b) generates +CR while a plait of opposite handedness (c) generates −CR. d-e) Light transmitted from the tip exhibits +CR for left-handed structures (d), and −CR for right-handed structures (e). Insets in d) and e) show a 2x magnification.

Simple linearly birefringent crystals can be assembled in microscopic helices that display both directional emission and rotation of the polarization plane of light. These results demonstrate the potential of bottom-up processes to organize simple building blocks across multiple length scales for complex functional materials.

Keyword self-assembly

Lukas Helmbrecht, Melissa Tan, Ruslan Röhrich, Marloes H. Bistervels, Bruno Ortiz Kessels, A. Femius Koenderink, Bart Kahr, Willem L. Noorduin*

Directed Emission from Self-Assembled Microhelices

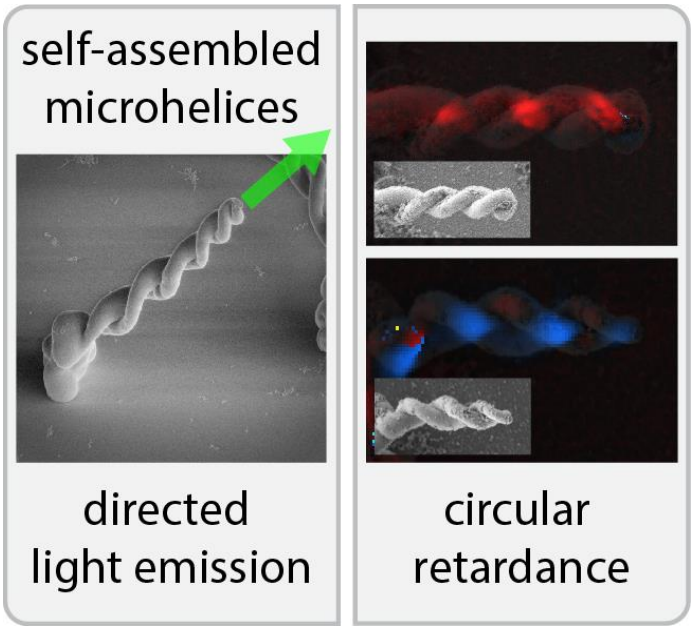

Supporting Information

Directed Emission from Self-Assembled Microhelices

*Lukas Helmbrecht, Melissa Tan, Ruslan Röhrich, Marloes H. Bistervels, Bruno Ortiz Kessels, Femius Koenderink, Bart Kahr, Willem L. Noorduin**

Content:

1. Fourier Microscopy for analyzing directional Emission of Microhelices

1.1 Fourier Microscopy Setup

The Fourier microscope consists of the following components: (Figure S1a)

- White light supercontinuum spectrally sliced to 490 nm, coupled to a multimode fiber (400 µm diameter) to achieve polarization scrambling and to avoid polarization dependent effects in the excitation of fluorescein. (SuperK EXTREME by NKT Photonics)
- Aperture to trim beam
- 470nm/40 Bandpass (BP) filter to remove white light tail form laser

- 10x air objective to focus the light at the base of the microhelix
- Fluorescent sample on X-Y stage
- 100x air objective while measuring, NA =0.9 (64.16° acceptance angle) (can be exchanged for a 10x objective during alignment)
- Beam splitter (removable) and white light source for white light imaging
- Telescope (2x 50 mm lenses) with 300 µm pinhole in between to select the tip of the microhelix and discard scattered light
- Two lenses to project image on CCD (one removable to switch between Fourier and real space)
- 2x long pass LP filter 500nm
- CCD (pco.panda 4.2 by PCO AG)

1.2 Data processing of Fourier images for directionality analysis

The direction of light emission from the microstructure is analyzed using the Fourier Microscopy setup (Figure S1a). The laser beam excites the fluorescent dye that is embedded in the helix. The beam originates from a white light supercontinuum that was spectrally sliced to 490 nm and fed through a multimode fiber, the end facet of which was then imaged onto the helix base. The multimode nature of the fiber together with the limited temporal coherence of the pump ensures that at the pump focus there is no preferred polarization orientation. For verification, upon testing with linear polarizers we indeed found no preferred pump polarization orientation, thereby excluding the polarization-dependence in fluorescein excitation.

Directional emission from the helix creates a light spot on the Fourier plane. The relation between that position and the emission angle is described by the Abbe sine condition for aplanatic systems: $r = f \sin\theta$ (Figure S1d). We define: r_E as the radial distance of the emission

peak from the center, Θ_{max} as the maximal acceptance angle of the objective, and r_{max} as the corresponding distance. Following the Abbe sine condition, the relation between the angle of emission Θ_E and the position of the emission on the Fourier plane is as follows:

$$\Theta_E = arcsin\left(\frac{r_E}{f}\right), \quad (1)$$

with $r_{max} = f\,NA$, follows:

$$\Theta_E = arcsin\left(\frac{r_E\,NA}{r_{max}}\right), \quad (2)$$

Alternatively:

$$\Theta_E = arcsin\left(\frac{k_E}{k_0}\right), \quad (3)$$

where k_E is the wave vector of the emission and $k_0 = 2\pi/\lambda_E$ the free space wave vector.

The emission direction is calculated using a computer script (Python) which crops the Fourier image to the region of interest, determines the location of the maximum intensity, and derives the corresponding angles using equation (3). Additionally, the script marks the position of emission as expected from the helix' geometry.

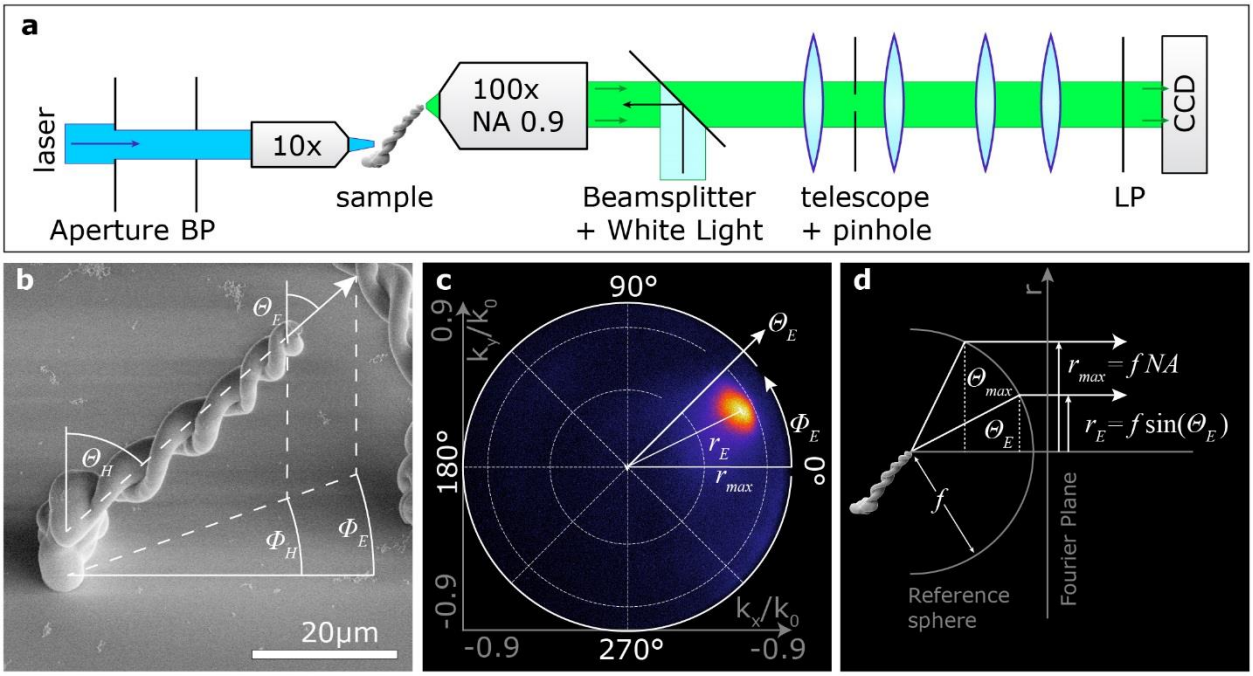

Figure S1. Fourier Microscopy Setup and Measurements. a) Fourier Microscope (details in section 3.1). b) SEM image with angles of orientation (Θ_H, Φ_H) and emission (Θ_E, Φ_E). c)

Measured Fourier image with r_E and r_{max} (see equations (1-3)). d) Schematic relation between the emission angle Θ_E and the position on the Fourier plane.

1.3 Additional Directionality Measurement

Supplementary to the specimen shown in Figure 2 in the main text we here present another example. In compliance with the previous microhelix, this one also shows a narrow emission angle and a good agreement between orientation and direction of emission (Figure S2).

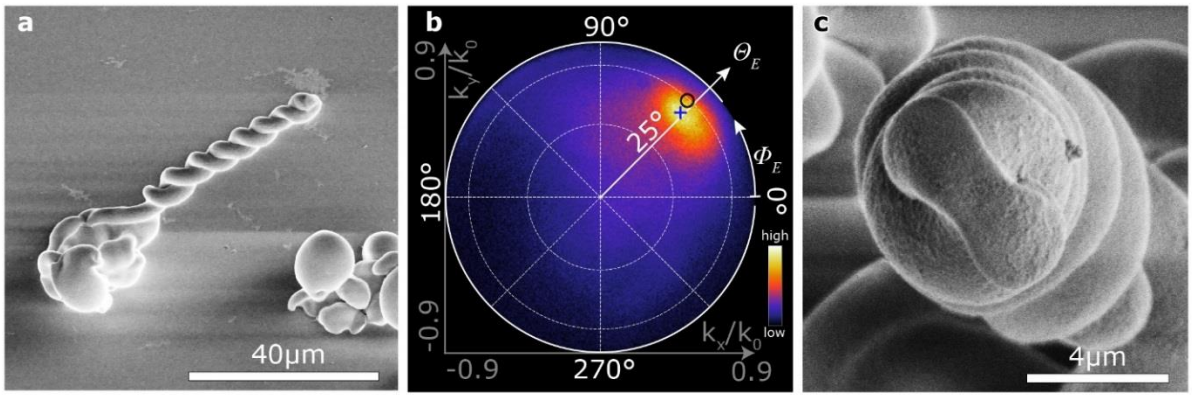

Figure S2. Directional light emission of a self-assembled microhelix. a) SEM image, and b) corresponding Fourier image of the emission, showing good agreement between orientation of the helix (marked with ○) and the direction of the emission (marked with +). c) Top view of the helix.

1.4 Analysis of the dispersion of the emission

The dispersion of the emission is determined from the spot size in the Fourier image. The boundary of this spot is obtained by applying a 1/e threshold. We measure a spot size of 23° in the Φ-direction and 15° in the Θ-direction for the helix in Figure 2 in the main text, therefore giving a beaming half angle of 11.5° and 7.5° respectively (Figure S3a).

In the simulation, a light field with a Gaussian profile was passed through a circular aperture with a 2 µm diameter and numerically propagated using the convolution-based Fresnel function in the "LightPipes" Python package to the back-focal plane of a lens with a 100 µm focal length. This small lens focal length was chosen in order to decrease the size difference between aperture and back-focal plane, which greatly reduces the resolution requirements and therefore the

simulation time. From the resulting intensity profile (Figure S3b), we derive a beaming half angle of 4°(Figure S3c).

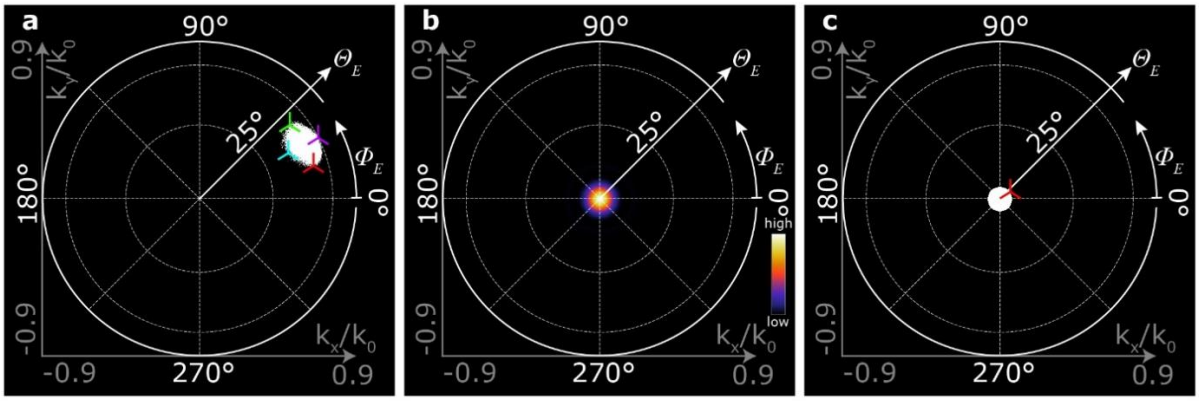

Figure S3. Analysis of the beaming half angle. a) Experimentally obtained spot size in the Fourier plane (1/e threshold is applied to the data of Figure S1c). The markers indicate the edges of the spot. The spread in the Φ-direction is 23° (green: Θ = 42°, Φ = 39°; red: Θ = 43°, Φ = 16°), and the spread in the Θ-direction is 15° (purple: Θ = 50°, Φ = 27°; cyan: Θ = 35°, Φ = 27). b) Simulated light field resulting from a 2µm aperture, c) applying a 1/e threshold shows a beaming half angle of 4°.

1.5 Mueller matrices

The concept of the dual rotating retarder Mueller matrix polarimeter was first described by Azzam in 1978.[28] Our system is built by modifying the accessory slots of an inverted commercial microscope frame (Zeiss Z1 Observer). In this design, monochromatic light, represented by the Stokes vector $S_{in} = [1\ 0\ 0\ 0]^T$, is transmitted through a linear polarizer ($\mathbf{P}_1$) coupled to a continuously rotating waveplate ($\mathbf{M}_{R1}$). Together, $\mathbf{P}_1$ and $\mathbf{M}_{R1}$ form the polarization state generator (PSG). After transmission through the sample, $\mathbf{M}_s$, light is gathered by an objective lens and sent to the polarization state analyzer (PSA), composed of a continuously rotating waveplate, $\mathbf{M}_{R2}$, followed by a fixed linear polarizer, $\mathbf{P}_2$. The continuous rotation of the waveplate elements creates a time-dependent signal at the detector that encodes for all 16 Mueller matrix elements, thereby, completely describing the polarization properties of a sample. The time-dependent scalar intensity signal measured at the detector can be represented as:

$$\mathbf{I}(t) = S_{\text{out}}\mathbf{P}_2\mathbf{M}_{\text{R2}}(t)\mathbf{M}_s\mathbf{M}_{\text{R1}}(t)\mathbf{P_1}S_{\text{in}}$$

Expansion of the scalar intensity function as a Fourier series reveals that $\mathbf{I}(t)$ has twelve frequency components.[28,31] If the period and frame rate are appropriately chosen, digital demodulation of the time varying signal recovers the complete Mueller matrix of the sample,

$$\mathbf{M}_S = \begin{bmatrix} m_{11} & m_{12} & m_{13} & m_{14} \\ m_{21} & m_{22} & m_{23} & m_{24} \\ m_{31} & m_{32} & m_{33} & m_{34} \\ m_{41} & m_{42} & m_{43} & m_{44} \end{bmatrix}.$$

The Mueller matrix was measured using a Mueller matrix microscope (Figure 3 main text). The circular retardance measurements shown in Figure 3 of the main text were obtained from the normalized Mueller matrix measurements shown in Figure S4.

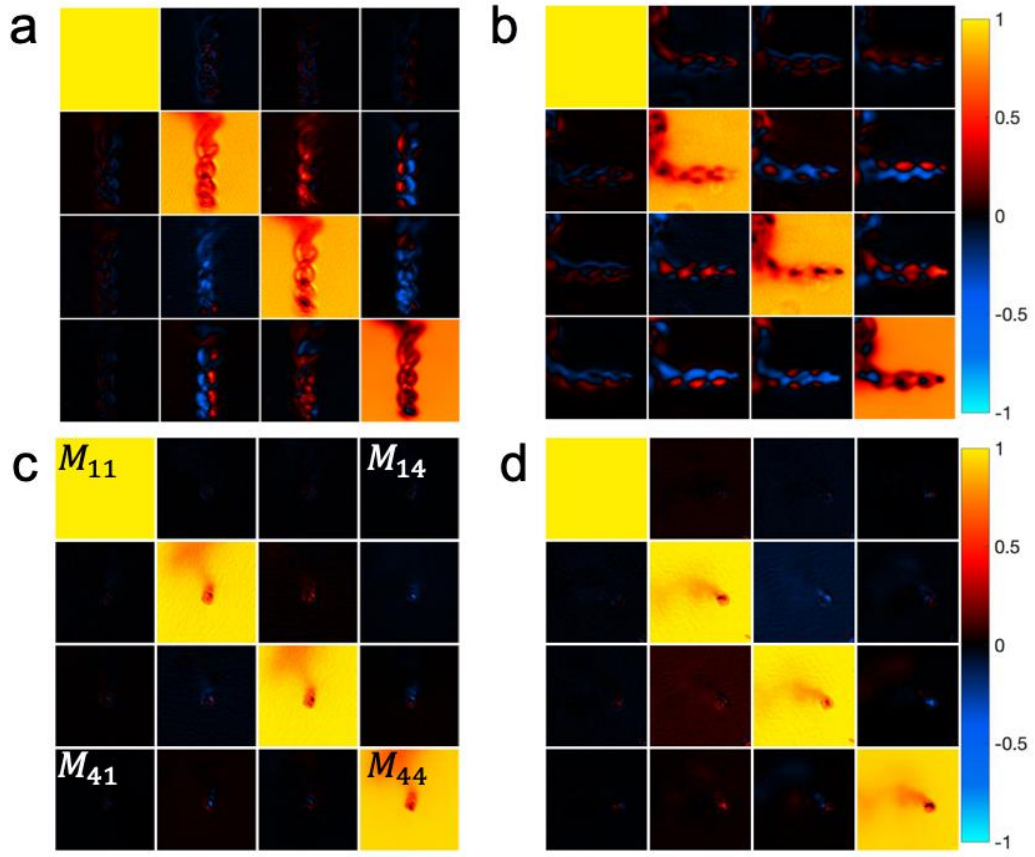

Figure S4. Normalized Mueller matrix measurements (transmission, λ=550 nm) of a left-handed helix (a and c) and a right-handed helix (b and d). The structures in a and b are laying flat on the substrate. Thus, the direction of light propagation is perpendicular to the long axis of the structure. In contrast, the helices in c and d are nearly orthogonal with respect to the substrate, and light is transmitted parallel to the long axis of the structure.